ADVANCED FUNCTIONAL MATERIALS
www.afm-journal.de

Reforming of Soluble Biomass and Plastic Derived Waste Using a Bias-Free $Cu_{30}Pd_{70}$|Perovskite|Pt Photoelectrochemical Device

*Subhajit Bhattacharjee, Virgil Andrei, Chanon Pornrungroj, Motiar Rahaman, Christian M. Pichler, and Erwin Reisner**

The production of clean fuels and chemicals from waste feedstocks is an appealing approach towards creating a circular economy. However, waste photoreforming commonly employs particulate photocatalysts, which display low product yields, selectivity, and reusability. Here, a perovskite-based photoelectrochemical (PEC) device is reported, which produces H_2 fuel and simultaneously reforms waste substrates. A novel $Cu_{30}Pd_{70}$ oxidation catalyst is integrated in the PEC device to generate value-added products using simulated solar light, achieving 60–90% product selectivity and ≈70–130 µmol cm^{-2} h^{-1} product formation rates, which corresponds to 10^2–10^4 times higher activity than conventional photoreforming systems. The single-light absorber device offers versatility in terms of substrate scope, sustaining unassisted photocurrents of 4–9 mA cm^{-2} for plastic, biomass, and glycerol conversion, in either a two-compartment or integrated "artificial leaf" configuration. These configurations enable an effective reforming of non-transparent waste streams and facile device retrieval from the reaction mixture. Accordingly, the presented PEC platform provides a proof-of-concept alternative towards photoreforming, approaching more closely the performance and versatility required for commercially viable waste utilization.

1. Introduction

The utilization of polymeric waste materials such as biomass, plastics, and industrial by-products for the generation of clean H_2 fuel and value-added products is a desirable approach towards a circular economy.[1–3] Photoreforming of abundant waste resources has emerged as a promising technology and relies on the excitation of a photocatalyst to oxidize the waste substrate, while simultaneously producing H_2.[3–6] Thus, photoreforming is unfolding as a complementary approach to other chemical recycling strategies such as pyrolysis or gasification of biomass and plastics, which are energy-intensive, rely often on relatively pure waste streams, and emit greenhouse gases.[7–9] In addition to H_2 generation, the waste substrates can be themselves photo-converted into value-added organic products, making the entire process economically more appealing.[3] However, the generation of these organic products suffers currently from significant drawbacks in terms of low product yield and uncontrolled oxidation, either emitting undesirable CO_2 or resulting in poor selectivity where a mixture of oxidation products is obtained that cannot be separated or utilized.[3–5,10] Thus, a major challenge lies in the development of an efficient oxidation co-catalyst to selectively transform the waste substrate in suspension.[11] Current approaches to photoreforming also mainly rely on the use of semiconductor powders, which challenge the optimization of the individual light-absorbing and catalytic components, and display low efficiency and recyclability from the residual solid waste.[3]

An alternative to semiconductor powder suspensions are photoelectrochemical (PEC) systems.[12] Lead halide perovskites have emerged as state-of-the-art light absorbers and recent encapsulation approaches have allowed for their integration in photoelectrodes.[13–16] Such PEC systems are known to perform water splitting[16] and CO_2 reduction,[14,15] but they usually require a tandem configuration with two different light absorbers to provide sufficient driving force for bias-free operation.[14,17,18] The less thermodynamically demanding oxidation of biomass and plastics eliminates in principle the strict requirement of a tandem PEC approach for efficient solar fuel synthesis and provides the basis for efficient solar energy conversion with a single light absorber.[3,19] Moreover, PEC systems can be leveraged to study the cathodic and anodic processes separately, which has the advantage of allowing for better screening and rational development of oxidation catalysts, which is not easily possible with photocatalyst powders, where both half-reactions occur at the same particle.[19]

S. Bhattacharjee, V. Andrei, C. Pornrungroj, M. Rahaman, C. M. Pichler, E. Reisner
Yusuf Hamied Department of Chemistry
University of Cambridge
Lensfield Road, Cambridge CB2 1EW, UK
E-mail: reisner@ch.cam.ac.uk

The ORCID identification number(s) for the author(s) of this article can be found under https://doi.org/10.1002/adfm.202109313.

DOI: 10.1002/adfm.202109313

Although a few reports exist on PEC H_2 evolution coupled to oxidation of organics, they either require an external bias, or show low photocurrent densities or efficiencies for waste conversion applications.[20–23]

Efficient waste conversion relies on a suitable oxidation catalyst that ultimately determines the performance of the system. The basic chemical building blocks of polymeric waste often consist of oxygenated substrates such as alcohols, aldehydes, and esters.[3,24] For example, ethylene glycol and glucose form a major component of poly(ethylene) terephthalate (PET) plastics[5] and lignocellulosic biomass,[10] respectively. While Pt and Pd-based catalysts offer high catalytic activities towards the required oxidation reactions,[25,26] Pd alloys with Cu exhibit an enhanced activity and increased poisoning tolerance over Pt in alkaline media.[27–31] However, inhomogeneity,[30,32] high synthesis temperatures,[29] and controlled composition[29] still pose challenges.

In this work, we probe the potential of PEC devices towards waste reforming. For this purpose, we first introduce and characterize bimetallic $Cu_{30}Pd_{70}$ alloy micro-flowers (MFs), which are developed as a selective waste oxidation catalyst. The catalyst is then combined with lead-halide perovskite photocathodes employing Pt as H_2 evolution catalyst (perovskite|Pt). These PEC devices are investigated in both two-compartment and "artificial leaf" configurations (see design in **Figure 1**a,b), in order to evaluate their performance towards light-driven, bias-free waste reforming. To establish the versatility of the combined $Cu_{30}Pd_{70}$|perovskite|Pt PEC systems, a wide variety of waste feedstocks such as glycerol, real world PET, and biomass-derived substrates are converted into clean H_2 and industrially relevant chemicals.[33–35] For example, glycolic acid (produced from PET) is used as a skin care agent in pharmaceutical industries.[33] Gluconic acid (produced from biomass-derived glucose) finds its use in the treatment of acid burns, anemia, etc.[34,35] The high rates and selectivity of these systems provide insights into the broader applicability of PEC technologies towards waste utilization.

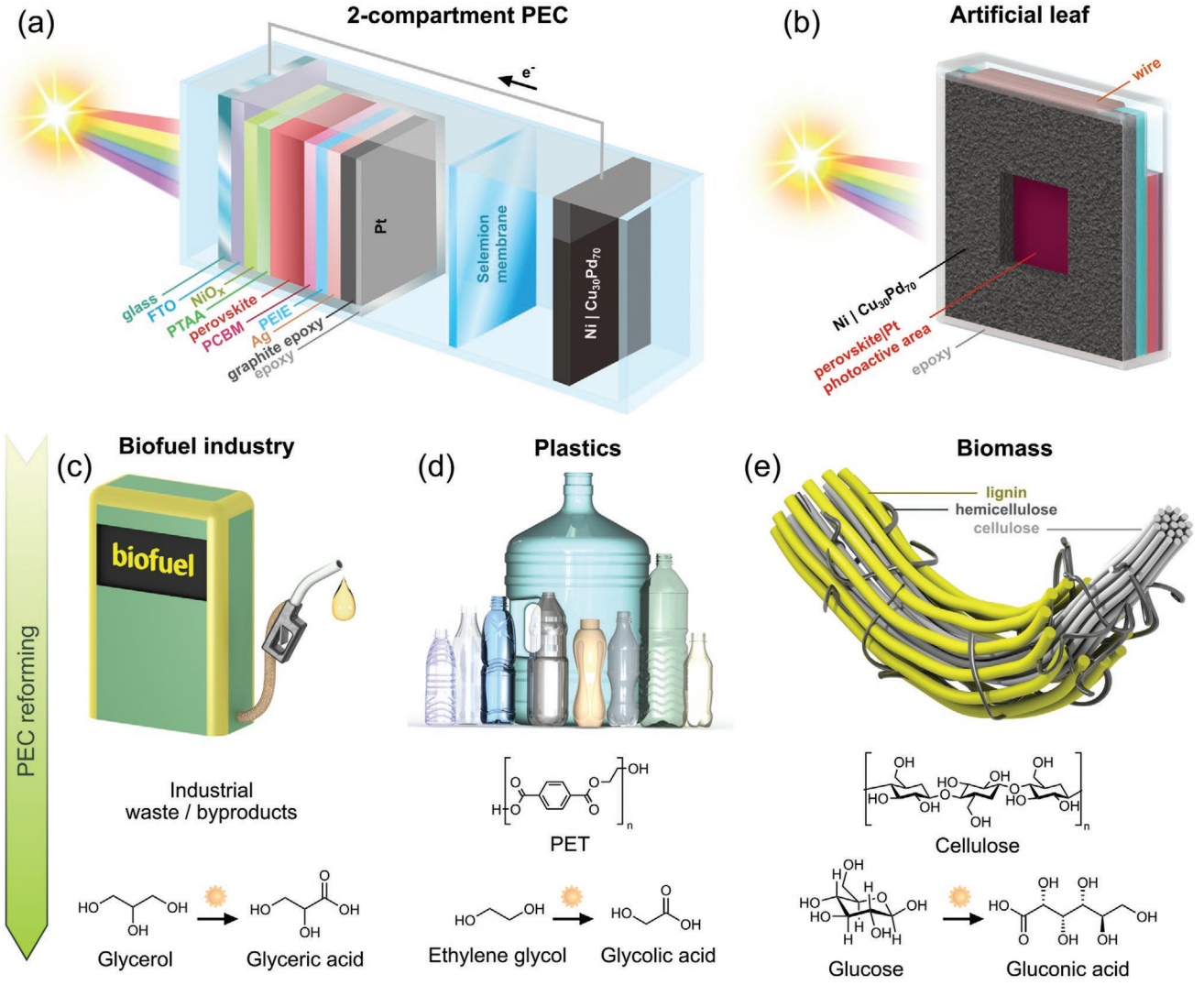

Figure 1. Overview of PEC waste reforming. a,b) Schematic depictions of the $Cu_{30}Pd_{70}$|perovskite|Pt system in two-compartment (a), and standalone "artificial leaf" configurations (b). c–e) Substrates for the PEC device with their corresponding major products. By-products of the biofuel industry such as glycerol (c). Plastics such as PET and its monomer ethylene glycol (d). Components of lignocellulosic biomass such as cellulose and its monomer glucose (e).

2. Results and Discussion

2.1. Preparation and Characterization of CuPd Alloy Catalysts

The physical separation of the oxidation and reduction reactions offered by a PEC configuration enables the individual catalyst development and process optimization for the oxidation half-reaction. For this purpose, mono and bimetallic systems were prepared on activated Ni foam (or graphite foil for characterization purposes) using a potentiostatic electrodeposition procedure (see Experimental Section for details).[36] In order to observe the effect of morphology and catalyst composition on the oxidation process, Cu, $Cu_{50}Pd_{50}$, $Cu_{30}Pd_{70}$, and Pd catalysts were synthesized. Field emission scanning electron microscopy (FESEM) images of the catalysts on Ni foam (**Figure 2**a and Figure S1, Supporting Information) show the change in morphology of the different systems as the Pd:Cu ratio is increased. Pristine Cu displays a dendritic branch-like morphology and a particle-like morphology appears rendering a flowery appearance to the system with the introduction of Pd. $Cu_{50}Pd_{50}$ displays a mixture of both dendritic branch-like and flower-like structures, whereas $Cu_{30}Pd_{70}$ predominantly exhibits a flower-like morphology with minor branching. Pure Pd exists in the form of small particles with little or no branching. $Cu_{30}Pd_{70}$

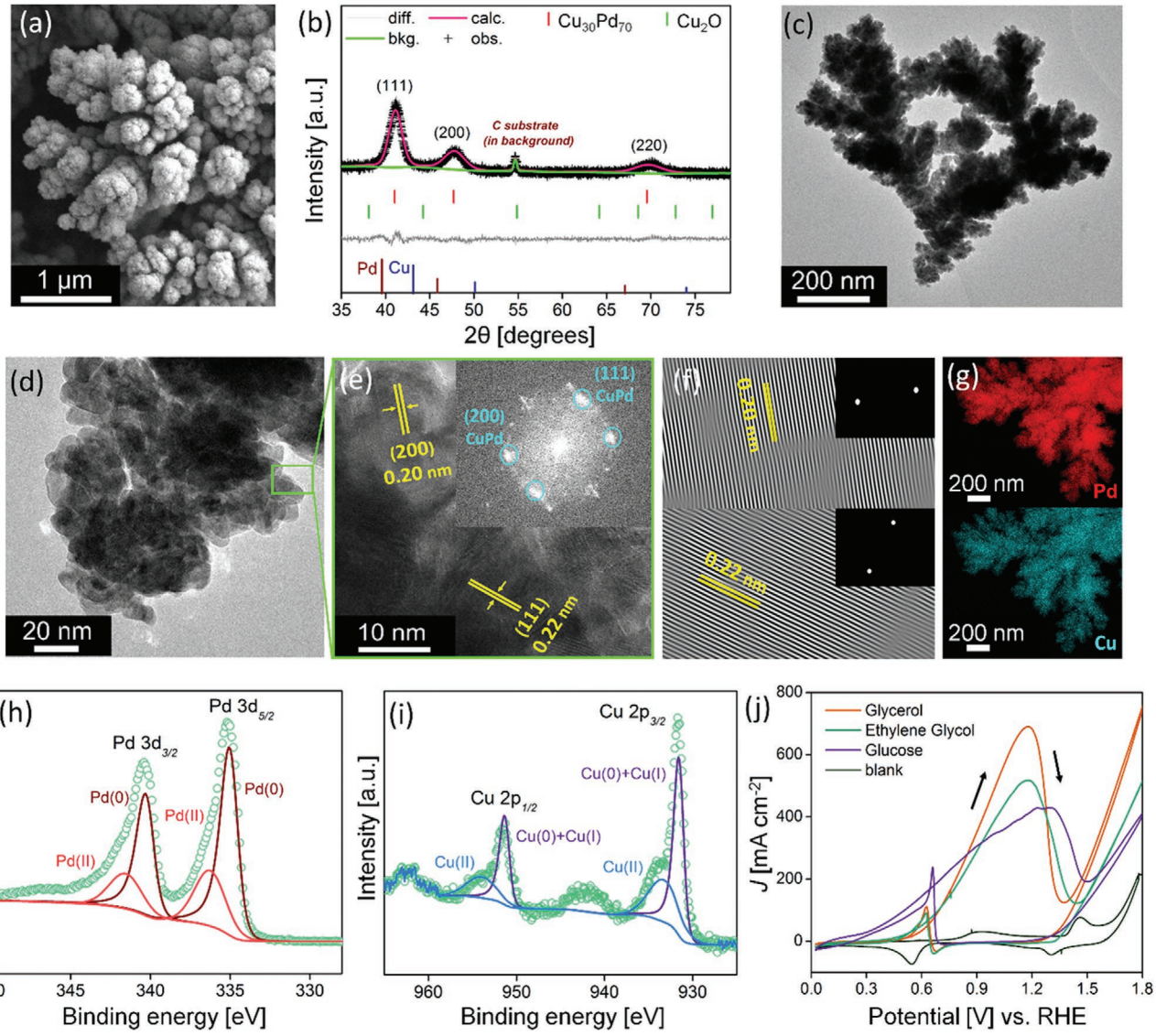

Figure 2. Characterization and electrochemistry of $Cu_{30}Pd_{70}$ MFs. a) FESEM image of $Cu_{30}Pd_{70}$ MFs. b) The PXRD pattern of $Cu_{30}Pd_{70}$ MFs and the corresponding Rietveld refinement. c,d) TEM image of the $Cu_{30}Pd_{70}$ MFs. e) HRTEM image of $Cu_{30}Pd_{70}$ showing the lattice fringes corresponding to (111) and (200) reflections. The inset shows the corresponding FFT patterns with the diffraction spots. f) The mask filtered HRTEM generated after inverse FFT used for calculating the *d*-spacing of the lattice fringes. The inset shows the corresponding masked FFT. g) STEM-mapping that shows Cu and Pd. h,i) Deconvoluted XPS spectra in the Pd *3d* region (h) and Cu *2p* region (i). j) CV scans with $Cu_{30}Pd_{70}$ MFs and different soluble model substrates (concentration: 0.5 M) recorded in a two-compartment electrochemical cell (three-electrode setup) in 1 M KOH electrolyte, 50 mV s^{-1} scan rate at room temperature with stirring.

shows the best performance among the catalysts (see below) and is, therefore, the focus of this study, herein referred to as $Cu_{30}Pd_{70}$ MFs.

The elemental composition of the $Cu_{50}Pd_{50}$ and $Cu_{30}Pd_{70}$ bimetallic systems was confirmed using energy dispersive X-ray spectral (EDX) mapping and inductively coupled plasma-optical emission spectrometry (ICP-OES) as shown in Figures S2 and S3, Supporting Information. The morphology and elemental composition of $Cu_{30}Pd_{70}$ MFs deposited on a graphite scaffold is identical and consistent with that of $Cu_{30}Pd_{70}$ MFs deposited on Ni foam (Figure S4, Supporting Information). The powder X-ray diffraction (PXRD) patterns of Cu, $Cu_{50}Pd_{50}$, $Cu_{30}Pd_{70}$, and Pd deposited on a graphite foil scaffold are shown in Figure S5, Supporting Information, and the Pd (111), (200), and (220) reflections shift towards higher 2θ with an increasing Cu content, which confirms the formation of a CuPd alloy.[37] Further information about the phases and lattice parameters of our main $Cu_{30}Pd_{70}$ MF system was obtained through Rietveld refinement, for which the PXRD pattern of the sample was taken after scratching it off from the scaffold (**Figure 2**b and Table S1, Supporting Information). The refinement revealed that the predominant phase is a $Cu_{30}Pd_{70}$ alloy with diffraction peaks at 41.03°, 47.69°, and 69.56° (corresponding to (111), (200) and (220) reflections, respectively), a cubic *fcc* (*Fm-3m*) crystal structure and a weight fraction of 0.912. The flower-like morphology of the $Cu_{30}Pd_{70}$ alloy is further confirmed by transmission electron microscopy (TEM) (Figure 2c,d). The d_{111} and d_{200} for $Cu_{30}Pd_{70}$ were estimated to be 0.22 and 0.20 nm, respectively from the high-resolution TEM (HRTEM) images (Figure 2e,f), which was also confirmed by the selected area electron diffraction (SAED) pattern (Figure S6a, Supporting Information). The scanning-TEM with high angle annular dark field (STEM-HAADF) image (Figure S6b, Supporting Information) and corresponding EDX maps of $Cu_{30}Pd_{70}$ (**Figure 2**g) further attested the compositional homogeneity and validated the elemental composition of the alloy. The TEM analysis for the $Cu_{50}Pd_{50}$ system is shown in Figure S7 (Supporting Information). X-ray photoelectron spectroscopy (XPS) survey analysis (Figure S8, Supporting Information) of the systems confirmed that no contamination or other heavy metals were present on the surface. The Cu $2p_{1/2}$, $2p_{3/2}$ and Pd $3d_{3/2}$, $3d_{5/2}$ from the respective Cu and Pd regions for $Cu_{30}Pd_{70}$ are shown in Figure 2h,i, confirming the existence of both metals on the surface (Figure S9, Supporting Information shows the deconvoluted XPS spectra for the $Cu_{50}Pd_{50}$ system). Traces of higher oxidation states are also observed and can be assigned to surface aerial oxidation.

2.2. Electrochemical Analysis

The electrochemical activity of the different catalyst systems towards substrate oxidation was first evaluated using a three-electrode setup with the catalyst electrodeposited on activated Ni foam as the working electrode, Ag/AgCl (sat. NaCl) as the reference electrode, Pt foil as the counter electrode in a 1 M aqueous potassium hydroxide (KOH) electrolyte solution. Cyclic voltammetry (CV) scans were employed to compare the electrochemical oxidation activity (Figure 2j and Figure S10, Supporting Information). For the initial screening, glycerol, ethylene glycol, and glucose were used with a concentration of 0.5 M in the working electrode compartment. Ethylene glycol and glucose are soluble model substrates for PET and cellulosic biomass, respectively, and glycerol is a waste by-product of the biodiesel industry (Figure 1).[38] The $Cu_{30}Pd_{70}$ MFs showed the highest electrocatalytic activity with a lower onset potential and higher current density for all three substrates as compared to pure Pd and $Cu_{50}Pd_{50}$ with pure Cu being inactive (Figure S10, Supporting Information). The onset potentials recorded for $Cu_{30}Pd_{70}$ were ≈0.4 V versus reversible hydrogen electrode (RHE) for glycerol and ethylene glycol, and ≈0.2 V versus RHE for glucose, with peak current densities of 688, 519, and 432 mA cm^{-2}, respectively. The control experiments with bare Ni foam and graphite are shown in Figure S11, Supporting Information, and show negligible current at potentials lower than 1.3 V versus RHE.

The high electrocatalytic activity of $Cu_{30}Pd_{70}$ MFs may be explained based on the optimum balance between the induced electronic changes due to alloying and dominance of active Pd sites. Besides, the $Cu_{30}Pd_{70}$ catalyst has a unique morphology with a controlled and homogenous elemental distribution (Figure 2g and Figures S2 and S3, Supporting Information). Introduction of Cu into the Pd lattice causes a down-shift in the *d*-band center of Pd, as reported previously using quantum mechanical tools.[39] This downward shift creates favorable adsorption dynamics of reactants on the $Cu_{30}Pd_{70}$ catalyst, thereby lowering the onset potential.[28,29] Cu, having optimum oxophilicity helps to adsorb OH^-, freeing active Pd sites for facile adsorption of substrates.[29,30] The OH_{ads} further aids the oxidation process and strips off the adsorbed intermediate species thereby reducing catalyst poisoning.[28,29] However, with the increase in Cu content, the number of Pd active sites decreases, and transport of substrates to Pd sites is also inhibited by a high concentration of OH_{ads} species.[29–31] Moreover, the roughness factor (R_F) determined for $Cu_{50}Pd_{50}$ (R_F = 60) is also lower than that of $Cu_{30}Pd_{70}$ (R_F = 140) (Figure S12, Supporting Information). These observations may explain the lower electrochemical activity for the $Cu_{50}Pd_{50}$ system, and hence, we did not proceed further with increasing the Cu percentage in our systems. Based on the electrochemical results and understanding,[39] the best performing $Cu_{30}Pd_{70}$ MFs were chosen as the oxidation catalyst for integration into our versatile PEC systems.

2.3. PEC Reforming of Soluble Model Substrates

The Ni foam|$Cu_{30}Pd_{70}$ anode (geometric surface area ≈ 1.5 cm^2) was next integrated with a perovskite|Pt cathode (≈0.25 cm^2 active area) in a two-compartment, two-electrode PEC configuration. The perovskite|Pt cathode was formed by sandwiching the hybrid organic-inorganic halide perovskite between electron and hole transporting layers (Figure S13, Supporting Information shows the cross-section FESEM of the cathode), and was then encapsulated before Pt deposition (see Experimental Section for details and Figure S14, Supporting Information, for optical images).[40] For the PEC measurements, the perovskite layer was back-illuminated through FTO-glass. The perovskite

devices achieved an average open circuit voltage (V_{oc}) of 1.08 ± 0.03 V (Figure S15, Supporting Information), and the perovskite|Pt photocathode irradiated with simulated solar light (AM 1.5G, 100 mW cm^{-2}) showed an onset potential of ≈1.0 V versus RHE for H_2 evolution in a three-electrode configuration (Figure S16a, Supporting Information).

The forward chopped CV scans in 1 M KOH solution in the two-electrode PEC configuration using the Ni foam|$Cu_{30}Pd_{70}$ anode connected to the perovskite|Pt photocathode showed onset voltages of ≈ –0.94, –0.91, and –1.04 V using glycerol, ethylene glycol, and glucose as substrate, respectively (**Figure 3**a with triplicates in Figures S17–S19, Supporting Information). The chronoamperometry (CA) measurements (Figure 3b) revealed average steady-state photocurrent densities of 7.4 ± 2.2, 7.6 ± 0.5, and 8.5 ± 0.9 mA cm^{-2} for glycerol, ethylene glycol, and glucose, respectively, at zero bias voltage. These photocurrents are consistent with the currents anticipated from the overlap of the individual CV curves in three-electrode measurements of perovskite|Pt under continuous illumination and Ni foam|$Cu_{30}Pd_{70}$ with the respective substrates shown in Figure S16b–d, Supporting Information.

While a stable photocurrent is maintained in the case of ethylene glycol and glucose, glycerol showed a gradual drop in photocurrent density with time possibly due to CO_{ads} poisoning generated upon C-C cleavage.[41] After 10 h of operation under bias-free conditions, 1083 ± 203, 1316 ± 269, and 1415 ± 314 µmol H_2 cm^{-2} were produced at the photocathode from the oxidation of glycerol, ethylene glycol, and glucose, respectively (Figure 3c). The corresponding Faradaic yields of H_2 (FY_{H2}) (Figure S20, Supporting Information) were above 90% and roughly constant throughout the experiments (Table S2, Supporting Information).

After completion of the PEC experiment, the anodic solution was analyzed using high-performance liquid chromatography (HPLC) for identification and quantification of the oxidation products (Figure 3d and Table S3, Supporting Information). The selectivities were calculated based on the H_2 yield and number of electrons transferred during the oxidation process. In case of glycerol, after a 10 h bias-free experiment, glyceric acid (111 ± 28 µmol) was identified as the major product with a selectivity of 79 ± 4% ($FY_{product}$ = 76 ± 7%). Ethylene glycol yielded 163 ± 45 µmol of glycolic acid with a high selectivity

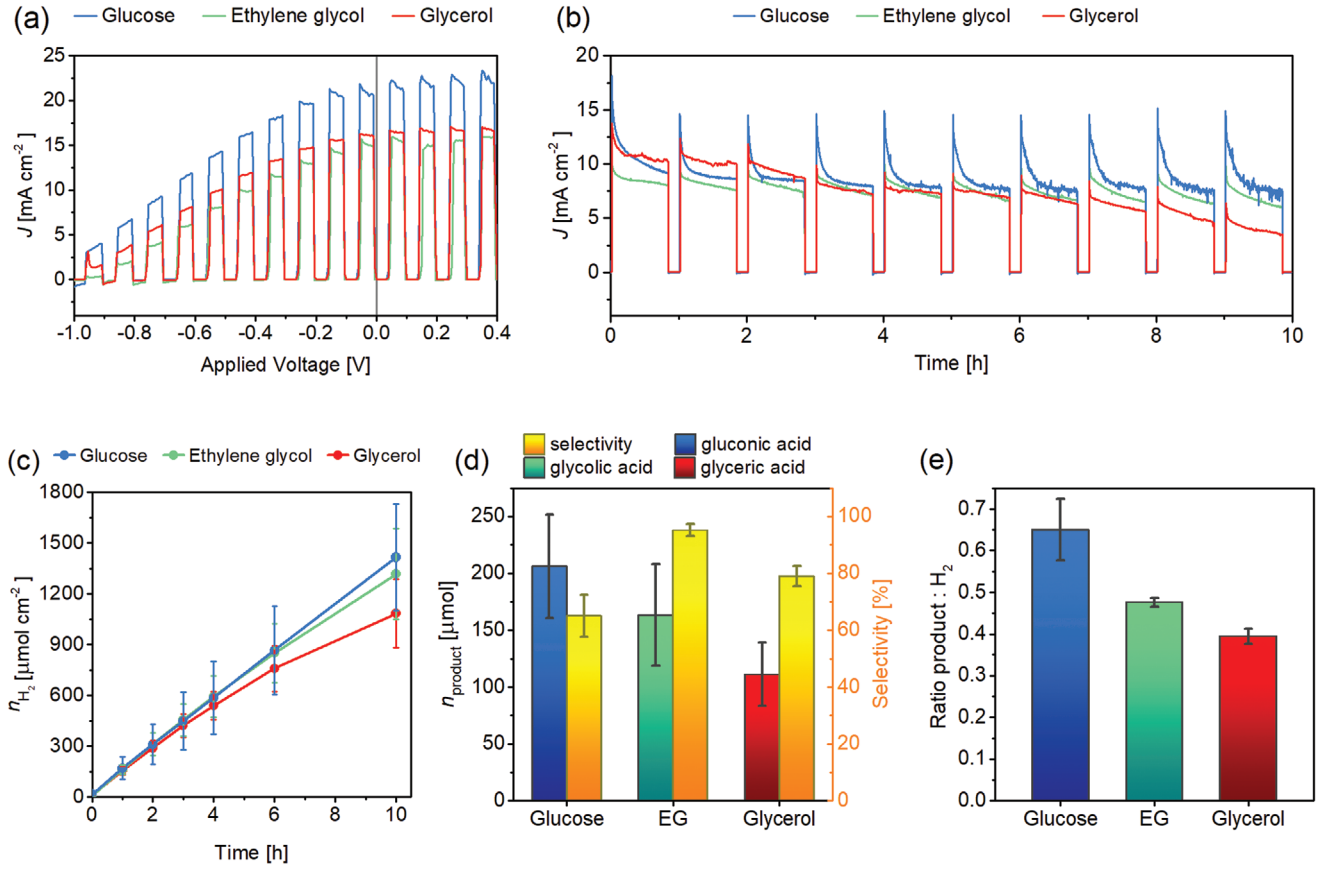

Figure 3. PEC with soluble model substrates. PEC responses using a two-compartment, two-electrode configuration (Ni foam|$Cu_{30}Pd_{70}$ anode connected to a perovskite|Pt photocathode) using glucose, ethylene glycol (EG), and glycerol as model substrates (0.5 M) recorded in 1 M KOH at room temperature with stirring in the "dark" anodic compartment. a) Forward CV scans (scan rate 10 mV s^{-1}) recorded under chopped simulated solar light irradiation (AM 1.5G, 100 mW cm^{-2}). b) The representative CA photocurrent densities for 10 h bias-free operation under 1 sun irradiation (50 min on, 10 min off) for the different substrates. c) The amount of H_2 produced at the cathode at different time intervals during the 10 h CA experiment at zero applied voltage. d) The amount of oxidation product formed from the respective substrates and the corresponding selectivity after 10 h of bias-free measurement. e) The oxidation product:H_2 ratio for the different substrates after 10 h bias-free measurement (theoretically predicted ratios are 1, 0.5, 0.5 for glucose, EG and glycerol conversion, respectively).

of 95 ± 2% ($FY_{product}$ = 91 ± 9%). Glucose, on the other hand, produced 206 ± 46 µmol of gluconic acid with a selectivity of 65 ± 7% ($FY_{product}$ = 63 ± 10%). Post catalysis FESEM and EDX analysis (Figure S21, Supporting Information) of the oxidation catalyst (with ethylene glycol substrate) confirmed the retention of the flower-like morphology and elemental composition, albeit minor agglomeration which is common in such type of electrodeposited systems.[17]

The overall high selectivity towards monoacid formation may be explained based on the CV overlap curves of perovskite|Pt under continuous illumination and Ni foam|$Cu_{30}Pd_{70}$ for different substrates (Figure S16, Supporting Information), and the V_{oc} (≈1 V versus RHE) provided by the perovskite. The overlap potentials for the different substrates (≈0.2–0.5 V versus RHE) correspond to a less positive working potential at the anode during bias-free operation, which prevents the formation of higher oxidation products. Moreover, in the solution phase, the high competition for active sites makes it difficult for the adsorbates to bind through more than one atom with the catalyst, favoring the conversion of only one hydroxyl group.[42] The results showed that glycerol and ethylene glycol are selectively oxidized via a 4-electron process to yield glyceric acid[43] and glycolic acid,[44] respectively (Figure S22a,b, Supporting Information). The process involves two successive oxidations of the alcohol group adsorbed on the CuPd surface. Glucose, however, undergoes a 2-electron oxidation process through the adsorption of C_1 aldehyde (from its open chain structure in solution) to give gluconic acid[45] as the major product during the PEC experiment (Figure S22c, Supporting Information). The high selectivity for ethylene glycol oxidation to glycolic acid may be attributed to the presence of only two carbon atoms and hence, lack of possible intermediates at low potentials. The lower selectivity for gluconic acid formation is possibly due to the alkaline degradation of glucose with time, isomerization, and other minor side reactions.[45,46] The ratio of oxidation product to H_2 (Figure 3e) roughly agreed with the expected ratio after 10 h of experiment; the oxidation product to H_2 ratio measured were 0.39 ± 0.02 for glycerol (theoretically 1:2, $2e^-.4e^-$ process), 0.48 ± 0.01 for ethylene glycol (theoretically 1:2, $2e^-.4e^-$ process), and 0.65 ± 0.07 for glucose (theoretically 1:1, $2e^-.2e^-$ process).

To gain further insights into the overall solar-driven process, the external quantum efficiency (EQE) spectrum (Figure S23a–c, Supporting Information and Table S4, Supporting Information) was determined for all the substrates at zero applied bias. Averaged EQE spectra were similar for different substrates plateauing around 70–80% over the visible region, which would correspond to an integrated current of ≈18 mA cm^{-2}. The spectra were comparable to those of perovskite PV devices, indicating that photocurrents are limited by mass transport and catalysis, rather than light absorption.[47]

2.4. PEC Reforming of Polymeric Substrates

PET powder, a real-world commercial PET bottle, and microcrystalline cellulose, which is a major component of lignocellulosic biomass were utilized for bias-free PEC measurements to demonstrate the capability to utilize waste polymer streams. While the PET powder and PET bottle were subjected to an alkaline pre-treatment method to hydrolyze the polymer to ethylene glycol and terephthalate,[5] cellulose was pre-treated by a multi-step mechanically-assisted procedure (see Experimental Section for details).[48] The pre-treated polymeric substrates were first studied in the two-compartment, two-electrode (Ni foam|$Cu_{30}Pd_{70}$ connected to perovskite|Pt) PEC system (Movie S1, Supporting Information, shows the H_2 evolution from the perovskite|Pt during the PEC measurements with pre-treated PET bottle). The forward chopped CV scans and CA traces for PET bottle and cellulose are shown in **Figure 4**a, whereas that of PET powder is shown in Figure S24a-b (Supporting Information), and chopped, light, and dark scans for all substrates are shown in Figure S25 (Supporting Information). The average steady-state photocurrent densities during the CA measurement (Figure 4b and Figure S24b, Supporting Information) under zero applied bias voltage were 5.2 ± 0.4, 4.7 ± 0.3, and 7.6 ± 2.3 mA cm^{-2} for PET powder, PET bottle, and cellulose, respectively.

After 10 h of experiment, the amounts of H_2 produced (Figure 4c) from pre-treated PET powder, PET bottle, and cellulose were 776, 748, and 1280 µmol cm^{-2}, respectively (Table S5, Supporting Information). The FY_{H2} (Figure S26a, Supporting Information) was above 90% throughout the measurement. The low H_2 yield for PET substrates as compared to pure ethylene glycol is due to the presence of terephthalate in the solution obtained after pre-treatment, which cannot effectively approach the electrode surface or may block the active sites and thereby inhibit catalysis.[5] Control experiments with only terephthalate (0.5 M) as substrate (Figure S27, Supporting Information) showed negligible photocurrent density (≈0.018 mA cm^{-2}) and H_2 production (2.4 µmol H_2 cm^{-2}) after 6 h at zero applied voltage. After 10 h, the PET powder and PET bottle produced 82 and 93 µmol of glycolic acid with a selectivity of 94% ($FY_{product}$ = 89%) and 91% ($FY_{product}$ = 88%), respectively (Figure 4d and Table S6, Supporting Information), which is comparable to the model substrates. Pre-treated cellulose produced 213 µmol of gluconic acid with 67% selectivity ($FY_{product}$ = 66%). The amount of oxidation product to H_2 ratio obtained were 0.47, 0.45, and 0.67 for PET powder, PET bottle, and cellulose, respectively (Figure S28a, Supporting Information). To the best of our knowledge, such high selectivities for transformation of plastics (e.g., real-world PET bottles) and biomass into higher-carbon chemicals have not yet been reported using photocatalytic or unassisted PEC approaches (Table S9, Supporting Information).[3]

2.5. Integrated Device with Polymeric Substrates

Integrated $Cu_{30}Pd_{70}$|perovskite|Pt "artificial leaf" devices were fabricated as a compact, robust system (Figure 1b), which can be directly immersed in the waste substrate solution to selectively produce H_2 and oxidation products utilizing solar energy without requiring any wiring or external bias (Figure S29 and Movie S1, Supporting Information). The integrated system was assembled by attaching the Ni foam|$Cu_{30}Pd_{70}$ to the perovskite|Pt photocathode. A window was made in the foam to irradiate the perovskite photoactive area (Figure 1b). The system was studied with the same polymeric waste substrates: PET powder, PET bottle, and cellulose. The chopped, light, and

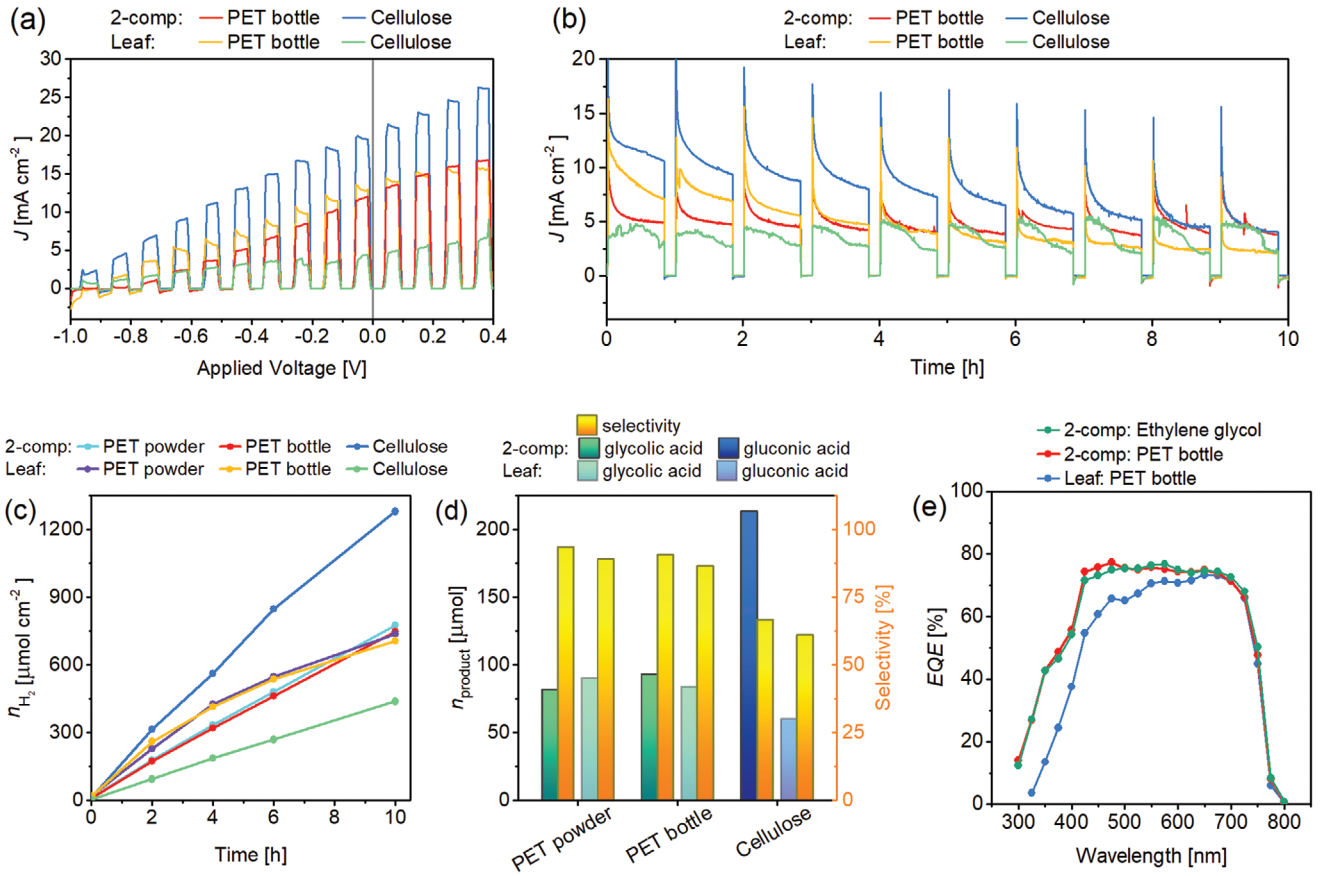

Figure 4. PEC with polymeric and real-world substrates. PEC responses in both two-compartment and "artificial leaf" configurations (Ni foam|$Cu_{30}Pd_{70}$ anode connected to a perovskite|Pt photocathode) using pre-treated polymeric and real-world substrates: PET powder, PET bottle, and cellulose, recorded in 1 M KOH at room temperature. The anodic substrate-containing solution in the two-compartment configuration is stirred, whereas no stirring is conducted for the integrated device. a) Forward CV scans (scan rate 10 mV s^{-1}) recorded under chopped simulated solar light irradiation (AM 1.5G, 100 mW cm^{-2}). b) Representative CA photocurrent densities for 10 h bias-free operation under 1 sun irradiation (50 min on, 10 min off) for the different substrates. c) The amount of H_2 produced at different time intervals during the 10 h CA experiment at zero applied voltage. d) The amount of oxidation product formed from the respective substrates and the corresponding selectivity after 10 h of bias-free measurement. e) EQE spectra of representative samples.

dark CV scans for all substrates are shown in Figure S30, Supporting Information. The photocurrent density of the "artificial leaf" in cellulose solution was ≈78% lower than in the two-compartment configuration (Figure 4a,b), which is likely due to light absorption and scattering through the yellow-colored, ball-milled cellulose solution (Figure S31, Supporting Information).[45,46,48] During the CA measurements (Figure 4b and Figure S24d, Supporting Information), a decrease in photocurrent density was observed in case of the pre-treated PET substrates. This may be attributed to the poisoning of Pt by intermediates and other species present in solution after pre-treatment, light scattering effects, or blockage of active sites by these species in the absence of stirring.[25,27] The steady-state photocurrent density observed was 5.1 ± 2.3, 4.6 ± 2.1, and 3.7 ± 0.3 mA cm^{-2} for PET powder, PET bottle, and cellulose, respectively during the 10 h CA measurement.

After 10 h, the amounts of H_2 evolved from PET powder and bottle were 737 and 705 µmol cm^{-2}, respectively (Figure 4c and Table S7, Supporting Information). The corresponding FY_{H2} was between 80–90% (Figure S26b, Supporting Information). Cellulose yielded 438 µmol cm^{-2} of H_2 (**Figure 4**c) with FY_{H2} in the 70–80% range throughout the experiment (Figure S26b, Supporting Information). As expected, the oxidation products obtained were similar with the two-compartment configuration, with PET powder giving 90 µmol of glycolic acid with 89% selectivity ($FY_{product}$ = 77%), PET bottle yielding 84 µmol of glycolic acid with 87% selectivity ($FY_{product}$ = 79%) and cellulose producing 60 µmol gluconic acid with 61% selectivity ($FY_{product}$ = 46%) (Figure 4d and Table S8, Supporting Information). The amount of product to H_2 ratios (Figure S28b, Supporting Information) measured were 0.45, 0.43, and 0.61 for PET powder, PET bottle, and cellulose, respectively. An "artificial leaf" device also displayed a promising reusability when operating over four 1-h cycles in different PET bottle solutions (Figure S32, Supporting Information) maintaining a fairly constant current density and steady H_2 production apart from the initial Pt poisoning. EQE spectra were employed to compare the performance of both device configurations with model substrates and real-world samples (Figure 4e and Figure S23d, Supporting Information). The EQE again

plateaued around 70–80% in the visible region for all investigated samples. A decrease in quantum efficiency was observed between 300–600 nm in the case of the one-compartment integrated "artificial leaf" device, due to light scattering at shorter wavelengths by the pre-treated PET solution.[49] These results successfully demonstrate the potential of solar-driven "artificial leaves", which can selectively reform waste substrates into industrially-relevant chemicals and simultaneously produce clean H_2 with high efficiency.

2.6. Comparison with Representative Systems

The transition from conventional suspension processes to unassisted PEC systems using a high-performance perovskite light absorber for waste reforming provides a significant advancement towards addressing the major existing bottlenecks such as low product yield (both H_2 and oxidation products) and uncontrolled oxidation leading to CO_2 emission or poor selectivity of the organic products.[3–6,10] Our approach addresses these challenges, as $Cu_{30}Pd_{70}$|perovskite|Pt systems showcase product formation rates of up to ≈130 µmol cm^{-2} h^{-1} (normalized to geometrical irradiation area), which are ≈10^2–10^4 times higher than previously reported photoreforming processes with established photocatalysts (**Figure 5**). Moreover, the high selectivity (60–90%) demonstrated by our systems towards the formation of a single value-added product, particularly for real-world substrates like PET bottles (≈90%), presents an attractive commercial advantage compared to typical photoreforming processes where only mixtures of non-utilizable products are obtained.[3–5,10] Thus, compared to conventional waste photoreforming, our approach provides a significant leap forward in terms of product formation rates, versatility, and selectivity, approaching some of the expected metrics for commercially viable waste utilization.[3]

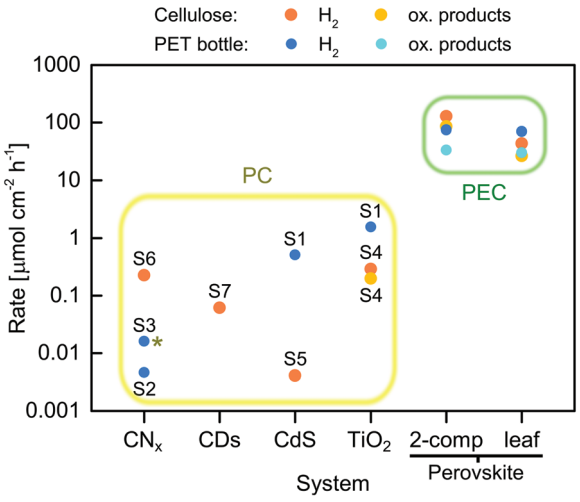

Figure 5. Comparison between representative photoreforming systems. The plot depicts the rate of product formation for conventional photocatalytic (PC) systems, and for the bias-free PEC reforming with $Cu_{30}Pd_{70}$ | perovskite | Pt devices using a real-world PET bottle and the polymeric biomass component cellulose (brown asterisk indicates a PC panel). The bias-free PEC systems display a 2–4 order of magnitude increase in the product rates over their PC counterparts (see Table S9, Supporting Information for further details and corresponding references; some entries are not plotted as the irradiation geometrical area has not been reported). Abbreviations: CN_x—"carbon nitride" and CDs—"carbon dots".

The two-compartment $Cu_{30}Pd_{70}$|perovskite|Pt system also provides further advantages. A dark mixed-waste solution can be utilized on the anodic side without blocking the light in the cathodic compartment, which is not possible in photocatalytic processes with homogenous or heterogenous photocatalysts.[6,10,11] This separation also enables a better optimization and rational development of the individual redox catalysts, which is challenging with semiconductor powders. Furthermore, the system can also be envisioned to perform other fuel forming reactions such as CO_2 reduction on the cathodic side instead of H_2 evolution, thereby increasing the product scope in future development.

In contrast to the requirement of tandem PEC cells in classical artificial photosynthesis, the replacement of O_2 evolution with a less thermodynamically challenging oxidation reaction eliminates the demand of a dual-light absorber PEC design for H_2 evolution or CO_2 reduction, enabling the construction of high-performance single light absorber PEC systems.

3. Conclusions

We have established PEC devices as an advantageous alternative towards light-driven waste valorization. To this end, we introduced a $Cu_{30}Pd_{70}$|perovskite|Pt system, which can generate clean H_2 and simultaneously produce useful value-added chemicals with high selectivity (60–90%) from a variety of waste feedstocks, attaining product formation rates of up to ≈130 µmol cm^{-2} h^{-1}, which are 10^2–10^4 times higher than conventional photocatalytic reforming. The versatile PEC system can operate in both two-compartment and integrated "artificial leaf" configurations under zero applied voltage. The former is particularly suitable for non-transparent waste streams and enables a decoupling of the oxidation and reduction processes, whereas a compact device arrangement facilitates its separation from a mixed waste solution. This proof-of-concept demonstration displays the benefits of PEC devices over existing photoreforming approaches, making strides towards widespread waste utilization. The development of commercial PEC systems may be facilitated by introducing scalable photocathode and catalyst deposition techniques, improving the device encapsulation, or using continuous flow systems.

4. Experimental Section

Materials: Palladium(II) chloride ($PdCl_2$ (59% Pd), anhydrous, Merck), copper(II) chloride ($CuCl_2$, anhydrous, 99%, ACROS), potassium hydroxide (KOH, 99.99%, semiconductor grade, Sigma-Aldrich), ethylene glycol (>99%, Sigma-Aldrich), glycerol (>99%, Sigma-Aldrich), D-(+)-glucose (>99.5%, Sigma-Aldrich), cellulose (micro-crystalline, Sigma-Aldrich), polyethylene terephthalate powder (PET, semi-crystalline, 30 µm, GoodFellow), nickel foam (1.6 mm thickness, MJ group), sulfuric acid (>95%, Fischer chemicals), FTO-coated glass (≈7Ω sq^{-1}, Sigma-Aldrich), hydrogen peroxide (H_2O_2, >30% w/v, Fisher), Zn (dust, 98+%, ACROS), hydrochloric acid (HCl, fuming, 36.5–38%, Honeywell), nickel nitrate hexahydrate ($Ni(NO_3)_2{\cdot}6H_2O$, ≥98.5%, Sigma-Aldrich), ethylenediamine (absolute, ≥99.5%, Fluka), lead iodide (PbI_2,

99.99%, trace metals basis, TCI), lead bromide ($PbBr_2$, for perovskite precursor, TCI), formamidinium iodide (Dyesol), methylammonium bromide (Dyesol), *N*,*N*-dimethylformamide (anhydrous, 99.8%, Sigma-Aldrich), 1-methyl-2-pyrrolidone (99.5%, extra dry over molecular sieves, ACROS), dimethyl sulfoxide (ACS reagent, ≥99.9%), chloroform (99.9%, extra dry over molecular sieves, stabilised, ACROS), PCBM (99%, Solenne BV), chlorobenzene (extra dry over molecular sieves ≥99.5%, ACROS), polyethylenimine (PEIE, 80% ethoxylated solution, 35–40 wt% in H_2O, average M_w 70 000, Sigma-Aldrich), 2-propanol (≥99.5%, Honeywell), poly(triarylamine) (average M_w 7000–10 000, Sigma-Aldrich), PTAA (M_w 17 700, EM INDEX), F4TCNQ (97%, Sigma-Aldrich), graphite powder (20 µm, Sigma-Aldrich), Araldite 5-Minute Rapid two component epoxy, Araldite Standard two component epoxy and a commercial sparkling water PET bottle were used without further purification unless otherwise stated.

Preparation of the Catalysts: A potentiostatic electrodeposition technique was used to fabricate the $Cu_{30}Pd_{70}$ MFs with high surface area and uniformity. The method has been adapted with small modifications from a previously reported procedure with a different alloy structure and combination.[36] For the preparation of $Cu_{30}Pd_{70}$ MFs, an electrodeposition bath was first prepared by dissolving $CuCl_2$ (85 mg), $PdCl_2$ (187 mg), and Na_2SO_4 (710 mg) in MilliQ water (50 mL). The solution was stirred under 600 rpm for several hours until homogeneity was observed. The optimized bath composition of metal precursors in this work was essential to obtain the desired metal composition in the alloy system. A three-electrode setup was used for the electrodeposition process, with the activated Ni foam (surface density 350 g m^{-2}, thickness 1.6 mm) as the working electrode, Pt foil as the counter electrode, and a leak-free Ag/AgCl (saturated NaCl) as the reference electrode. The Ni foam was activated by sonicating in 2 M HCl, MilliQ water, and ethanol, respectively for 5 min in each and drying under N_2 flow, prior to electrodeposition. The electrodeposition process was carried out in the prepared electrodeposition bath at −0.8 V versus Ag/AgCl (saturated NaCl) for 600 s. After electrodeposition, the catalyst was dipped in MilliQ water for 10 s and dried under a gentle flow of N_2.

For the $Cu_{50}Pd_{50}$ alloy, the electrodeposition bath was prepared by dissolving 142 mg $CuCl_2$ (142 mg), $PdCl_2$ (112 mg), and Na_2SO_4 (710 mg) in MilliQ water (50 mL). The Cu and Pd control systems comprised of $CuCl_2$ (226 mg) and $PdCl_2$ (299 mg), respectively in MilliQ water (50 mL). The total number of moles of the metallic precursors in the electrodeposition bath was kept constant for all the systems. For some characterization techniques, graphite foil was used as the electrode scaffold instead of Ni foam in order to avoid the interference of Ni and facilitate easy scratching of the catalyst from the scaffold. Prior to electrodeposition, the graphite scaffold was activated by sonication in water-acetonitrile mixture (1:1 v/v) for 10 min, followed by drying at 50 °C under air.

Preparation of Inverse Structure Perovskite: The inverse structure triple cation mixed halide perovskite devices were prepared according to the previously reported method with minor modifications.[14,40] Briefly, a NiO_x hole-transporting layer (HTL) was uniformly deposited on FTO-coated glass via spin-coating of 1 M $Ni(NO_3)_2{\cdot}6H_2O$, 1 M ethylenediamine solution in ethylene glycol. The FTO-coated glass was then subjected to annealing treatment at 573 K. A second HTL was added over the NiO_x layer by spin coating F4TCNQ-doped PTAA solution inside an N_2-filled glove box. A cesium formamidinium methylammonium (CsFAMA) perovskite precursor solution was prepared by first making 1000 µL of $FAMA_{0.22}Pb_{1.32}I_{3.2}Br_{0.66}$ solution in DMF (510 µL), DMSO (340 µL), and 1-methyl-2-pyrrolidone (150 µL), to which 48 µL of 1.5 M CsI in DMSO was added. A two-step spin coating procedure with first 10 s at 1000 rpm and next 35 s at 6000 rpm was then employed to deposit a smooth perovskite film onto the PTAA layer, using chloroform as the antisolvent ≈7 s before the end of spin-coating. The perovskite layer was further subjected to anneal treatment at 373 K for 30 min. For the electron transporting layer (ETL), a [6,6]-phenyl C_{61} butyric acid methyl ester (PCBM) solution (35 mg mL^{-1} in chlorobenzene) was spin-coated over the perovskite film at 3000 rpm for 45 s. Next, in order to prevent interfacial degradation owing to reaction with metal contact, a PEIE film was deposited on top of the PCBM coated perovskite layer by spin coating PEIE solution (3.9 µL mL^{-1}) in isopropanol at 3000 rpm for 30 s. Finally, a 100 nm conductive Ag layer was deposited by metal evaporation through a patterned mask, ensuring an active perovskite area of ≈0.5 × 0.5 cm^2.

Encapsulation and Preparation of Perovskite|Pt Cathodes: Graphite powder was homogeneously mixed with epoxy (Araldite Standard 2 component epoxy) in a 3:4 graphite:epoxy mass ratio to form a conductive graphite epoxy (GE) paste. This paste was then evenly spread on top of the Ag contact layer of the perovskite device. The Ag layer serves as an electrical contact between the perovskite and the encapsulating GE paste. The GE was then allowed to harden for 24 h, after which the edges of the device were sealed using Araldite 5-min Rapid two component epoxy. Finally, a 5 nm Pt film, was deposited onto the GE layer using magnetron sputtering. Figure S14, Supporting Information, shows the photographs of the prepared perovskite|Pt cathodes.

Fabrication of $Cu_{30}Pd_{70}$|Perovskite|Pt "Artificial Leaf" Systems: For the fabrication of "artificial leaf" systems, the $Cu_{30}Pd_{70}$ MFs were first deposited on Ni foam window (open area ≈0.275 cm^2) with an active area of ≈1.3 cm^2. A Cu wire was then welded to this oxidation catalyst to provide contact. Thereafter, the oxidation catalyst was carefully adhered to the FTO-glass side of perovskite|Pt with rapid epoxy aligning the window with the active perovskite illumination area. Figure S29, Supporting Information, shows the photographs of a prepared $Cu_{30}Pd_{70}$|perovskite|Pt "artificial leaf".

Material Characterization: The PXRD measurements were performed using a Panalytical X'Pert Pro (K alpha Cu radiation) diffractometer from 2θ of 30° to 80°. The PXRD was performed for the samples electrodeposited on graphite scaffold. For the Rietveld analysis of the main $Cu_{30}Pd_{70}$ sample, the PXRD measurement was performed at a slow 2θ scan rate of 1° min^{-1} of the material scratched off from the scaffold after electrodeposition as the refinement requires minimal influence from the scaffold for higher accuracy and better convergence. GSAS-II software was used for the Rietveld refinement of the PXRD pattern wherein the descending values of weighted average residual (R_{wp}) and goodness of fit (GOF) values were tracked to ascertain the quality of refinement. The resultant crystallographic information file (CIF) generated was used to visualize the unit cell(s) using VESTA software. The FESEM was performed using a TESCAN MIRA3 FEG-SEM instrument equipped with an Oxford Instruments Aztec Energy X-maxN 80 EDX system. A Thermo Scientific Talos F200X G2 TEM (FEI, operating voltage 200 kV) was used for the TEM image acquisition, HR-TEM, STEM-HAADF, elemental mapping and SAED analysis. The Tecnai Imaging and Analysis (TIA) software was used to extract the fast Fourier Transform (FFT) patterns, and a mask filter was applied to omit the undesired lattice planes. Thereafter, the impression of the single desired lattice plane was obtained by applying inverse-FFT of masked FFT patterns. The XPS of the system was performed at the Maxwell Centre, University of Cambridge with a near ambient pressure (NAP) XPS system which uses a SPECS XR 50 MF X-ray source, µ-FOCUS 600 X-ray monochromator and a differentially pumped PHOIBOS 150 1D-DLD NAP analyzer. The peak positions were calibrated with respect to the C1s peak at ≈286 eV. The curve fitting and deconvolution were performed using a Casa-XPS software. The ICP-OES measurements were performed at Microanalysis Service, Yusuf Hamied Department of Chemistry, University of Cambridge on a Thermo Scientific iCAP 7400 ICP-OES DUO spectrometer.

Pre-Treatment of Polymeric and Real-World Substrates: An alkaline pre-treatment method was adopted for the PET substrates.[5] Briefly, a solution of commercial PET powder in 1 M KOH (50 mg mL^{-1}) was heated to 80 °C for 96 h under stirring. Thereafter, the solution was kept undisturbed at room temperature to cool and allow the unreacted PET to settle down. The supernatant was directly taken for the PEC experiments. The concentration of ethylene glycol after pre-treatment of PET powders was ≈15 ± 3 mg mL^{-1} (≈0.2 M) as determined by HPLC. For studies using real world PET, a sparkling water bottle made of

PET was cut into smaller pieces, dipped in liquid nitrogen, and then pulverized in a grinder. The grinded PET bottle was then subjected to the same alkaline pre-treatment process, but for a longer duration (120 h) to ensure sufficient depolymerization. The final concentration of ethylene glycol, in this case, was ≈13 ± 1 mg mL^{-1} (≈0.2 M).

For the pre-treatment of cellulose, which is a primary component of biomass, a solvent-free, mechanically-assisted depolymerization approach was used.[48] Cellulose (10 g) was first dispersed in diethyl ether (150 mL) containing 9.2 mmol H_2SO_4. The suspension was stirred for 1 h, followed by removal of the solvent under reduced pressure. The fine white powder obtained was then processed in a ball mill containing ZrO_2 balls of size 3 mm. The ball-milling was performed at 400 rpm for 20 h (10 min mill, 20 min rest). The acid-impregnated cellulose obtained after ball milling was then hydrolyzed to yield glucose monomers. In a stainless-steel autoclave, an aqueous solution of ball-milled acid impregnated cellulose (10 wt%) was heated at 130 °C for 1 h under stirring. The solution was then filtered and stored for further use. The concentration of glucose in the final solution was determined using HPLC and found to be ≈8.4 ± 0.4 mg mL^{-1} (≈0.05 M). Prior to the PEC measurements, aqueous KOH was added to the monomer solution placed in an ice bath to adjust the pH to 14.

Electrochemical Measurements: The electrochemical measurements were performed using an Ivium CompactStat Electrochemical Analyzer in a three-electrode setup. A two-compartment cell separated by a Selemion anion exchange membrane, with the reference electrode in the working electrode compartment, was used for the tests with 1 M KOH as the electrolyte. 0.5 M of glycerol, ethylene glycol, and glucose were used as model substrates to test the oxidation reactions individually. Cu_xPd_y alloy catalysts deposited on activated Ni foam were used as the working electrode for substrate oxidation, whereas a Pt foil and Ag/AgCl (saturated NaCl) were used as the counter electrode and reference electrode, respectively. The CV scans were performed at 50 mV s^{-1} scan rate at room temperature under stirring. The current obtained was normalized with respect to the geometrical surface area of the working electrode. Unless otherwise stated, all the potentials reported have been converted from the Ag/AgCl (saturated NaCl) scale to RHE scale using the following equation:

$$E_{(\mathrm{RHE})} = E_{(\mathrm{Ag/AgCl})} + 0.197\ \mathrm{V} + 0.059 \times \mathrm{pH} \tag{1}$$

The roughness factor (R_F) for the different catalysts was determined using capacitance measurements. Steady-state CV scans were taken at different scan rates (10, 25, 50, 100 mV s^{-1}) in the non-faradaic region in 1 M KOH aqueous electrolyte solution. The slope of the current versus the scan rate gives the double layer capacitance (C_{dl}), which was used to estimate the R_F. For comparison, the R_F of the blank Ni foam substrate was taken as unity.[50]

PEC Measurements: For the PEC measurements, a Newport Oriel 67005 solar light simulator was used with an Air Mass 1.5 Global (AM 1.5G) solar filter. A certified Newport 1916-R optical power meter was used for the calibration of light intensity to 100 mW cm^{-2} (1 Sun) before each PEC experiment. All PEC measurements were conducted using a CompactStat potentiostat with Ni foam|$Cu_{30}Pd_{70}$ (effective area 1.5 cm^2) as the anode and perovskite|Pt as the photocathode, where the perovskite layer was back-illuminated. For the two-compartment, two-electrode bias-free PEC measurements, 1 M aqueous KOH was used as the electrolyte solution and the anodic and cathodic compartments were separated using a Selemion anion exchange membrane. The cell was sealed with rubber septa and the solutions on both sides were purged with N_2 (with 2% methane internal standard) for 25 min prior to the PEC measurements. The purging needle holes were then sealed using Loctite superglue Universal adhesive.

Studies using soluble model substrates glycerol, ethylene glycol, and glucose were carried out by dissolving the substrate in 1 M KOH to reach a concentration of 0.5 M in the anodic compartment. However, pre-treated solution of PET powder and real-world PET bottle in 1 M KOH was directly used in the anodic compartment for the oxidative substrate reforming process. The alkaline pH was conducive for improving the catalytic activity of the oxidation reaction on Pd-Cu alloys due to the presence of OH_{ads} species, helping to maintain high photocurrent densities and sufficient working potential (≈0.2–0.4 V versus RHE as shown in the CV overlap plots between Ni foam|$Cu_{30}Pd_{70}$ anode and perovskite|Pt photocathode: Figure S16, Supporting Information) during the bias-free measurements.[28–30] Reducing the pH to neutral conditions would result in a poor overlap between CV scans, thereby decreasing the overall driving force in bias-free operation.[29,30] In case of microcrystalline cellulose, the pre-treated solution adjusted to pH 14 using KOH was used directly in the anodic compartment. In all the experiments, the pH of both the compartments was kept constant (1 M KOH) with no chemical bias in the form of additional redox non-innocent reagents.

The CV scans (chopped, light, and dark) were performed at a scan rate of 10 mV s^{-1}. The long term 10 h CA scans were performed under chopped light irradiation (50 min of, 10 min off) at zero bias. The photocurrents were normalized to the photoactive area of the perovskite. All the experiments were conducted at room temperature. In case of the "artificial leaf" configuration, the PEC tests were carried out in a single sealed compartment with the respective pre-treated polymeric substrate solutions in 1 M KOH under no stirring. The EQE measurements were done using a LOT MSH-300 monochromator, a Thorlabs PM100D power meter with a Thorlabs S302C thermal power sensor, and an Ivium CompactStat potentiostat. The wavelength (FWHM 15 nm) was varied between 300 and 800 nm in 25 steps every 30 s. The EQE values were determined using Equation (2), where h is the Planck constant, c is the speed of light, J is the photocurrent density, e is the electronic charge, λ is the wavelength, and P_λ is the wavelength-dependent light intensity flux.

$$\mathrm{EQE}\,(\%) = \frac{hcJ}{e\lambda P_\lambda} \times 100 \tag{2}$$

Product Detection and Quantification: The amount of H_2 evolved from the perovskite|Pt cathode was detected and quantified by manual injection from the PEC cell headspace into a Shimadzu GC-2010 Plus gas chromatograph (GC) and quantified using methane as the internal standard.[40] The chromatographic separations for oxidation products were conducted with a Phenomenex Rezex 8% H+ column at 75 °C column temperature. Samples were analyzed in the isocratic flow mode (flow rate 0.0025 M H_2SO_4 in water, 0.5 mL min^{-1}) using a Waters breeze system equipped with refractive index (RID-2414) and diode array UV–vis (λ = 202 nm)[51] detectors. In order to identify particular substances in the reaction samples, retention times were compared to those of authentic samples. The selectivity of the products formed was calculated using Equation (3), where *n[formed]* is the number of moles of oxidation product formed after 10 h of experiment and *n[expected]* is the expected number of moles of oxidation product calculated from the amount of H_2 evolved and number of electrons involved. The theoretical oxidation product to H_2 ratio is considered to be 2:1 and 1:1 for a 4-electron and 2-electron oxidation process, respectively as H_2 evolution is a 2-electron process.

$$\mathrm{Selectivity}\,(\%) = \frac{\mathrm{n[formed]}}{\mathrm{n[expected]}} \times 100 \tag{3}$$

The Faradaic yields of the products were calculated using Equation (4), where Z is the number of electrons transferred to generate the product, n is the number of moles of product formed, F is the Faraday constant (96485 C) and Q_{passed} is the total charge passed during the same time interval.

$$\mathrm{FY[product]}\,(\%) = \frac{ZnF}{Q_{\mathrm{passed}}} \times 100 \tag{4}$$

All the PEC measurements were performed in triplicates, except for the tests with polymeric samples in which PET powder and PET bottle have

the same composition and yielded similar concentration of ethylene glycol monomers after pre-treatment. Cellulose pre-treatment, on the other hand, involves a series of steps and multiple hydrolysis reactions to yield enough volume of solution containing glucose monomers for a single PEC experiment. The average values are based on triplicates and the errors correspond to the standard deviation of data points from individual samples.

Supporting Information

Supporting Information is available from the Wiley Online Library or from the author.

Acknowledgements

This work was supported by the Cambridge Circular Plastics Centre (CirPlas, EP/S025308/1) and the Hermann and Marianne Straniak Stiftung. S.B., V.A. and C.P. are grateful to the financial support from the Cambridge Trust (HRH The Prince of Wales Commonwealth Scholarship to S.B.; Vice-Chancellor's Award to V.A.; Cambridge Thai Foundation Award to C.P.). V.A. also acknowledges financial support from the Winton Programme for the Physics of Sustainability, Cambridge Philosophical Society, Trinity College and St John's College. C.P. also acknowledges the Trinity-Henry Barlow Scholarship. M.R. acknowledges the financial support for a Marie-Sklodowska-Curie Individual European Fellowship (SolarFUEL, GAN 839763) and C.M.P. acknowledges the financial support from Austrian Science Fund (Schrödinger Fellowship J-4381). The authors thank S. Verma, Dr. S. Dey and Prof. C. Grey (University of Cambridge) for help with the ball-milling and Dr. H. Greer (University of Cambridge) for helping with the TEM measurements. The authors are grateful to Dr. S. Linley, Dr. D. Antón-García and Dr. T. Uekert (University of Cambridge) for useful feedback on the manuscript.

Conflict of Interest

The authors declare no conflict of interest.

Data Availability Statement

Raw data related to this article are available at the University of Cambridge data repository: https://doi.org/10.17863/CAM.76598.

Keywords

biomass, perovskite, plastic, reforming, solar fuels

Received: September 28, 2021
Published online:

[1] *IEA 2019*, OECD, Paris Cedex 16 https://doi.org/10.1787/1e0514c4-en.
[2] S. van Renssen, *Nat. Clim. Change* **2020**, *10*, 799.
[3] T. Uekert, C. M. Pichler, T. Schubert, E. Reisner, *Nat. Sustain.* **2021**, *4*, 383.
[4] V. Nguyen, D. B. Nimbalkar, L. D. Nam, Y. Lee, H. Teng, *ACS Catal.* **2021**, *11*, 4955.
[5] T. Uekert, H. Kasap, E. Reisner, *J. Am. Chem. Soc.* **2019**, *141*, 15201.
[6] J. Ma, D. Jin, Y. Li, D. Xiao, G. Jiao, Q. Liu, Y. Guo, L. Xiao, X. Chen, X. Li, J. Zhou, R. Sun, *Appl. Catal., B* **2021**, *283*, 119520.
[7] S. B. Borrelle, J. Ringma, K. Lavender Law, C. C. Monnahan, L. Lebreton, A. McGivern, E. Murphy, J. Jambeck, G. H. Leonard, M. A. Hilleary, M. Eriksen, H. P. Possingham, H. De Frond, L. R. Gerber, B. Polidoro, A. Tahir, M. Bernard, N. Mallos, M. Barnes, C. M. Rochman, *Science* **2020**, *369*, 1515.
[8] J. M. Garcia, M. L. Robertson, *Science* **2017**, *358*, 870.
[9] J. Zheng, S. Suh, *Nat. Clim. Change* **2019**, *9*, 374.
[10] D. S. Achilleos, W. Yang, H. Kasap, A. Savateev, Y. Markushyna, J. R. Durrant, E. Reisner, *Angew. Chem., Int. Ed.* **2020**, *59*, 18184.
[11] C. Y. Toe, C. Tsounis, J. Zhang, H. Masood, D. Gunawan, J. Scott, R. Amal, *Energy Environ. Sci.* **2021**, *14*, 1140.
[12] J. H. Kim, D. Hansora, P. Sharma, J. W. Jang, J. S. Lee, *Chem. Soc. Rev.* **2019**, *48*, 1908.
[13] I. Poli, U. Hintermair, M. Regue, S. Kumar, E. V. Sackville, J. Baker, T. M. Watson, S. Eslava, P. J. Cameron, *Nat. Commun.* **2019**, *10*, 2097.
[14] V. Andrei, B. Reuillard, E. Reisner, *Nat. Mater.* **2020**, *19*, 189.
[15] H. Zhang, Y. Chen, H. Wang, H. Wang, W. Ma, X. Zong, C. Li, *Adv. Energy Mater.* **2020**, *10*, 2002105.
[16] I. S. Kim, M. J. Pellin, A. B. F. Martinson, *ACS Energy Lett.* **2019**, *4*, 293.
[17] M. Rahaman, V. Andrei, C. Pornrungroj, D. Wright, J. J. Baumberg, E. Reisner, *Energy Environ. Sci.* **2020**, *13*, 3536.
[18] Gurudayal, D. S. , M. H. Kumar, L. H. Wong, J. Barber, M. Grätzel, N. Mathews, *Nano Lett.* **2015**, *15*, 3833.
[19] W. Yang, R. R. Prabhakar, J. Tan, S. D. Tilley, J. Moon, *Chem. Soc. Rev.* **2019**, *48*, 4979.
[20] M. T. Bender, X. Yuan, K. S. Choi, *Nat. Commun.* **2020**, *11*, 4594.
[21] D. Liu, J. C. Liu, W. Cai, J. Ma, H. Bin Yang, H. Xiao, J. Li, Y. Xiong, Y. Huang, B. Liu, *Nat. Commun.* **2019**, *10*, 1779.
[22] D. V. Esposito, R. V. Forest, Y. Chang, N. Gaillard, B. E. McCandless, S. Hou, K. H. Lee, R. W. Birkmire, J. G. Chen, *Energy Environ. Sci.* **2012**, *5*, 9091.
[23] H. G. Cha, K. S. Choi, *Nat. Chem.* **2015**, *7*, 328.
[24] K. Sanderson, *Nature* **2011**, *474*, S12-S14.
[25] J. Xie, P. Duan, N. Kaylor, K. Yin, B. Huang, K. Schmidt-Rohr, R. J. Davis, *ACS Catal.* **2017**, *7*, 6745.
[26] X. Zhao, M. Yin, L. Ma, L. Liang, C. Liu, J. Liao, T. Lu, W. Xing, *Energy Environ. Sci.* **2011**, *4*, 2736.
[27] Y. Kim, Y. Noh, E. J. Lim, S. Lee, S. M. Choi, W. B. Kim, *J. Mater. Chem. A* **2014**, *2*, 6976.
[28] Z. Chen, Y. C. He, J. H. Chen, X. Z. Fu, R. Sun, Y. X. Chen, C. P. Wong, *J. Phys. Chem. C* **2018**, *122*, 8976.
[29] T. Hu, Y. Wang, H. Xiao, W. Chen, M. Zhao, J. Jia, *Chem. Commun.* **2018**, *54*, 13363.
[30] K. Jiang, P. Wang, S. Guo, X. Zhang, X. Shen, G. Lu, D. Su, X. Huang, *Angew. Chem., Int. Ed.* **2016**, *55*, 9030.
[31] O. Muneeb, J. Estrada, L. Tran, K. Nguyen, J. Flores, S. Hu, A. M. Fry-Petit, L. Scudiero, S. Ha, J. L. Haan, *Electrochim. Acta* **2016**, *218*, 133.
[32] Y. Cheng, J. Xue, M. Yang, H. Li, P. Guo, *Inorg. Chem.* **2020**, *59*, 10611.
[33] E. R. Valle-González, J. A. Jackman, B. K. Yoon, N. Mokrzecka, N, N. J. C. , *Sci. Rep.* **2020**, *10*, 7491.
[34] S. Ramachandran, P. Fontanille, A. Pandey, C. Larroche, *Food Technol. Biotechnol.* **2006**, *44*, 185.
[35] D. Thomas, U. Jaeger, I. Sagoschen, C. Lamberti, K. Wilhelm, *Cardiovasc. Intervent. Radiol.* **2009**, *32*, 155.
[36] H. B. Noh, K. S. Lee, P. Chandra, M. S. Won, Y. B. Shim, *Electrochim. Acta* **2012**, *61*, 36.
[37] M. Rahaman, K. Kiran, I. Z. Montiel, V. Grozovski, A. Dutta, P. Broekmann, *Green Chem.* **2020**, *22*, 6497.
[38] A. A. Abdul Raman, H. W. Tan, A. Buthiyappan, *Front. Chem.* **2019**, *7*, 774.
[39] F. Fouda-Onana, O. Savadogo, *Electrochim. Acta* **2009**, *54*, 1769.
[40] C. Pornrungroj, V. Andrei, M. Rahaman, C. Uswachoke, H. J. Joyce, D. S. Wright, E. Reisner, *Adv. Funct. Mater.* **2021**, *31*, 2008182.
[41] A. C. Garcia, M. J. Kolb, C. Van Nierop Y Sanchez, J. Vos, Y. Y. Birdja, Y. Kwon, G. Tremiliosi-Filho, M. T. M. Koper, *ACS Catal.* **2016**, *6*, 4491.

[42] M. B. Griffin, A. A. Rodriguez, M. M. Montemore, J. R. Monnier, C. T. Williams, J. W. Medlin, *J. Catal.* **2013**, *307*, 111.
[43] Z. Zhao, J. Arentz, L. A. Pretzer, P. Limpornpipat, J. M. Clomburg, R. Gonzalez, N. M. Schweitzer, T. Wu, J. T. Miller, M. S. Wong, *Chem. Sci.* **2014**, *5*, 3715.
[44] J. X. Tang, Q. S. Chen, L. X. You, H. G. Liao, S. G. Sun, S. G. Zhou, Z. N. Xu, Y. M. Chen, G. C. Guo, *J. Mater. Chem. A* **2018**, *6*, 2327.
[45] G. Moggia, T. Kenis, N. Daems, T. Breugelmans, *ChemElectroChem* **2020**, *7*, 86.
[46] D. J. Maclaurin, J. W. Green, *Can. J. Chem.* **1969**, *47*, 3947.
[47] V. Andrei, R. L. Z. Hoye, M. Crespo-Quesada, M. Bajada, S. Ahmad, M. De Volder, R. Friend, E. Reisner, *Adv. Energy Mater.* **2018**, *8*, 1801403.
[48] N. Meine, R. Rinaldi, F. Schüth, *ChemSusChem* **2012**, *5*, 1449.
[49] W. R. Krigbaum, T. Tanaka, *Macromolecules* **1988**, *21*, 743.
[50] M. Rahaman, A. Dutta, A. Zanetti, P. Broekmann, *ACS Catal.* **2017**, *7*, 7946.
[51] S. Solmi, C. Morreale, F. Ospitali, S. Agnoli, F. Cavani, *ChemCatChem* **2017**, *9*, 2797.